Research paper

Low-temperature and high-pressure phase transitions in 1-decyl-3-methylimidazolium nitrate ionic liquid

Hiroshi Abe [a], [*], Yuto Yoshiichi [a], Hiroaki Kishimura [a], Hajime Sagayama [b]

[a] Department of Materials Science and Engineering, National Defense Academy, Yokosuka 239-8686, Japan
[b] Institute of Materials Structure Science, High Energy Accelerator Research Organization (KEK), Tsukuba 305-0801, Japan

ARTICLE INFO

ABSTRACT

The phase behavior of 1-decyl-3-methylimidazolium nitrate ($[C_{10}mim][NO_3]$) was investigated at a low temperature (LT) under ambient pressure and a high pressure (HP) under ambient temperature. $[C_{10}mim][NO_3]$ is an ionic liquid (IL) possessing a long alkyl chain length. Detailed crystal structures of the IL at LT and HP were determined by synchrotron radiation experiments. The weak Bragg reflections in the low wavevector (Q) region were clearly observed. At LT, the Bragg reflection at the lowest Q was positioned differently than the prepeak in the liquid state. The 00ℓ Bragg reflections at $Q_{00\ell}$ indicate a hybrid-layered structure with a lattice constant of 4.3 nm. In addition to the 00ℓ Bragg reflections, the double peak occurred in the region of Q_{002} at HP; thus new HP crystal structures were observed in $[C_{10}mim][NO_3]$.

1. Introduction

Flexible metal–organic frameworks (MOFs) have been investigated at low temperature (LT) and high pressure (HP) [1–7]. The flexibility of the pore space-tunable MOFs indicated a large pore to narrow pore phase transition with changing their molecular conformation. The MOF-like crystal polymorphs were observed in ionic liquids (ILs). The ILs consisting of a cation and an anion are characterized by nanoheterogeneity even in the liquid state [8,9]. The representative cation is 1-alkyl-3-methyl imidazolium, $[C_n mim]^+$, where n indicates the alkyl chain length. Nanoheterogeneity is developed depending on the alkyl chain length of the cations. Moreover, in $[C_n mim][X]$, phase diagrams as a function of n were determined at LT [10–12]. At LT, IL-based liquid crystals (LCs) appeared in large n. In addition, LCs are synthesized to regulate the dimensionality of the mesoscopic organization [13–21]. For instance, cylinder and layered LCs are easily self-assembled on the mesoscopic scale. One-dimensional (1D) and two-dimensional (2D) morphologies are tuned using the anisotropic motifs. For instance, micelles, vesicles, lamellar, hexagonal, and cubic morphologies are self-organized. The photochromic properties in the functionalized ILs have been reported for applications [22,23]. Moreover, IL-based LC complexes have been developed as mechanical actuators [24], and the frequency dependence of the deflection has also been determined.

The crystal structures of ILs reveal the molecular interactions of a cation and an anion. The crystal structures have been determined to es-timate the ion pair interactions, including hydrogen bonding. At HP, the hybrid-layered structure with stacking and folding layers appeared as the specific crystal structures under ambient temperature [25]. The hybrid-layered structure is entirely different from the LC-based layered structure. Moreover, crystal polymorphs and multiple pathways of the phase transitions have been clarified at LT under ambient pressure and HP under ambient temperature [26–35]. The conformational polymorph and packing polymorph both influence the complex phase behavior; the conformational polymorph corresponds to conformational flexibility. Density functional theory (DFT) calculations have revealed that the conformational degrees of freedom increase as the alkyl chain length increases [36]. Raman spectroscopy revealed a link between the conformational changes of the cation and anion and the crystal polymorphs at LT under ambient pressure [37]. The packing efficiency is significant in the phase transitions at HP under ambient temperature. Benzocaine, one of the commercially available drugs, indicates the HP crystal polymorph at ambient temperature [38]. A hydrogen-bonded ribbon of benzocaine plays a crucial role as a motif for the packing polymorph.

Molecular dynamics (MD) has been used to simulate $[C_n mim][NO_3]$ nanostructures [39–41]; the predicted crystal structures are for $n = 4$, 6, 8, 10, and 12. Moreover, solid–solid phase transitions, including the LC phases, have been demonstrated. The layered structures for $n = 8$, 10, and 12 show a weak interaction between the polar layers and higher-ordered alkyl chain orientation. The simultaneous measure-

ments of X-ray diffraction and differential scanning calorimetry have been used to investigated the LT phase behavior of $[C_{10}mim][NO_3]$ [42]. It was found that the cooling rates extensively influence phase transitions, and the multistep phase transition has been observed as a quasi-equilibrium state at the intermediate cooling rate.

In this study, we used synchrotron radiation experiments to investigate the phase behavior of $[C_{10}mim][NO_3]$ at LT under ambient pressure and HP under ambient temperature. Complex crystal structures were observed with large lattice constants; however distinct crystal polymorphs were found at LT and HP.

2. Experimental section

The IL used in this study was hydrophilic $[C_{10}mim][NO_3]$, which was purchased from Angene Chemical Co. Vacuum drying was conducted for 48 h.

On the BL-8B beamline of the Photon Factory at the High-Energy Accelerator Research Organization (KEK) in Japan, LT powder X-ray diffraction at ambient pressure was performed utilizing a high-speed spinner to remove the preferred orientation of the Debye rings. 2D diffraction patterns were obtained using a cylindrical imaging plate (IP) system (R-AXIS, Rigaku Co.). The liquid sample was placed in the 0.3 mm-diameter quartz capillary tube. The cooling system used was GN2-SN (Rigaku Co.), with cooling and heating rates of 2 K/min. The scattering wavevector Q was defined as $4\pi(\sin\theta)/\lambda$ (nm^{-1}), where the scattered angle was 2θ. The incident wavelength ($\lambda = 0.1378$ nm) was calibrated using a CeO_2 polycrystalline standard.

HP X-ray diffraction experiments at ambient temperature were carried out using a Mao–Bell-type diamond anvil cell (DAC) in the BL-18C of the Photon Factory at KEK [43]. The sample and ruby balls were loaded into the hole (diameter, 0.30 mm) of the pre-indented stainless

gasket (thickness, 0.15 mm) in the DAC, under a dry-flowing helium atmosphere in a glove bag. A microbeam of diameter 35 μm was obtained using double collimators, and 2D diffraction patterns were obtained using an IP system (BAS2500, Fuji-Film Co., Japan) [43]. IP was set at distance of 166.4 mm for X-ray diffraction. The 2D data were converted into 1D intensity data to minimize the preferred orientation on the Debye rings. A vacuum chamber with polyimide (Kapton)-film windows (125 μm thickness) was used to eliminate air scattering. The pressure was determined from the spectral shift of the R_1 fluorescence line of the ruby balls placed in the sample chamber of the DAC. The scattered angles 2θ and the incident wavelength, λ ($= 0.08293$ nm), were calibrated using a standard CeO_2 polycrystalline.

The observed X-ray diffraction patterns were analyzed using the *CONOGRAPH* software [44] and the *ab initio* structure determination program in *FOX* [45]. *CONOGRAPH* determined the crystal system and lattice parameters. In addition, the molecular arrangements in the unit cell were simulated using *FOX*, using global optimization algorithms.

3. Results

3.1. LT phase behavior of $[C_{10}mim][NO_3]$ at ambient pressure

Fig. 1(a) and 1(b) show the LT phase transitions of $[C_{10}mim][NO_3]$ at cooling and heating rates of 2 K/min. The black and colored curves in Fig. 1(a) and 1(b) correspond to the observed and calculated X-ray diffraction patterns, respectively. Over the whole Q region, the calculated diffraction patterns including the weak Bragg reflections were reproducible. A prepeak appeared at 2.4 nm^{-1} (Q_{pre}) in the liquid (L) phase at room temperature, which shifted to the lower Q position with decreasing temperature. At 250 K (T_{C1}), the sharp Bragg reflections indicate the crystallization of $[C_{10}mim][NO_3]$, and this phase is defined
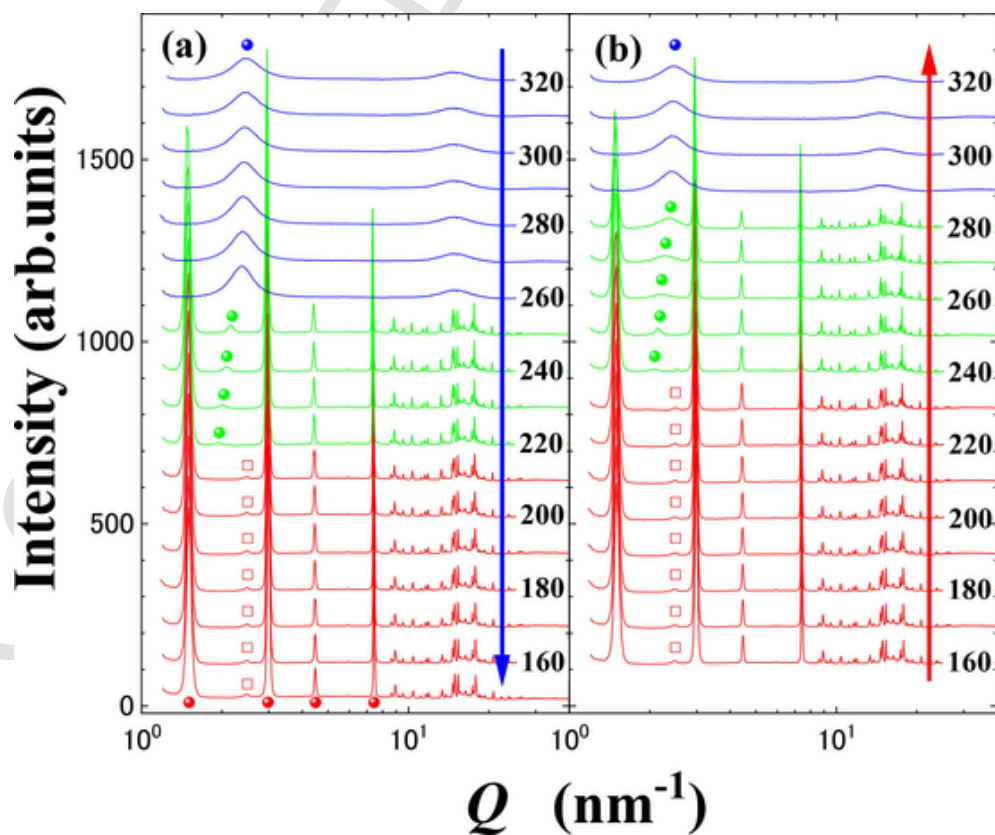

Fig. 1. Temperature dependences of X-ray diffraction patterns in $[C_{10}mim][NO_3]$ upon (a) cooling, and (b) heating. Blue and green closed circles reveal the prepeak position (Q_{pre}) and Q_{LC} of a liquid crystal-like layered structure, respectively. Red closed circles indicate the 00ℓ Bragg reflections exhibiting the hybrid-layered structure. The red open square indicates the Q_2 peak in the C_{II} phase. The numbers in the figure reveal temperatures (K).

as C_I. The ideal Debye rings of the C_I phase were obtained on the IP. The sharp but weak Bragg reflection denoted by the green closed circle (Fig. 1(a)) was observed at 2.2 nm^{-1} (Q_{LC}), close to the prepeak position (Q_{pre}). In a previous study [42], the weak Bragg reflection was ambiguous using the in-house X-ray generator. The Bragg peak is derived from the LC-like layered structure. In addition to the Q_{LC} Bragg peak, the 00ℓ Bragg reflections appeared at $Q_{00\ell}$, as indicated by the red closed circles (Fig. 1(a)). The 001 Bragg reflection was positioned at 1.5 nm^{-1} (Q_{001}), which is lower than Q_{LC}, indicating that the hybrid-layered structure was formed in LT [C_{10}mim][NO_3] in the same way as HP [C_{10}mim][Cl] was formed in the previous study [25]. The Bragg reflection at Q_{LC} shifted continuously to 2.0 nm^{-1} with decreasing intensity from 250 K to 220 K. Here, we emphasize that the peak shift of the weak Bragg reflection at Q_{LC} was extracted by the synchrotron radiation experiments. This is in contrast to the normal temperature dependency of lattice constants. In general, Q shifts to higher Q positions at LT, reflecting on the smaller lattice constants, whereas, the Q_{LC} shifting to the lower Q means that the lattice modulations become opposingly large. In addition, the $Q_{00\ell}$ positions were slightly dependent on the temperature. In case of the peak shifting of the Q_{hk0} Bragg reflections at the high Q region, lattice contraction on the ($hk0$) planes occurred with decreasing temperature. The crystal structure of the C_I phase at 220 K was determined to be tetragonal (Table 1). It should be noted that the crystal structure of [C_{10}mim][NO_3] was wrongly determined to be monoclinic [42]; the number of Bragg reflections was too small due to the weak incident X-ray from the in-house X-ray source. In the present study, a lot of sharp Bragg reflections without the preferred orientation of the Debye rings provide the right crystal structures at LT. P422 (tetragonal) was identified as one of the possible space groups using the global optimization method. However, the exact molecular configuration of the C_I phase was not determined uniquely due to a relatively limited number of Debye rings and a large molecular size of [C_{10}mim]$^+$ in the large unit cell. The long stacking sequence of $c = 4.2$ nm corresponds to the 00ℓ Bragg reflections. Fig. S1(a) illustrates one of the possible hybrid-layered structures of the C_I phase. The layered structure at 220 K is expressed in the unit cell. Further cooling resulted in a phase transition at 210 K (T_{C2}) and the disappearance of the Q_{LC} Bragg peak. Here, the new phase (C_{II} phase) was identified by the additional weak Bragg reflections (Fig. 1(a)). For instance, one of the weak peaks denoted by the red open square in Fig. 1(a) appeared at 2.5 nm^{-1} (Q_2), where the peak position had little temperature dependence below T_{C2}. The temperature invariance of Q_2 peak was detected for the first time in this study using the synchrotron radiation experiments. The Q_2 peak was closely positioned to Q_{pre}. The C_{II} phase was found to be orthorhombic from structure analysis, and its crystallographic parameters were obtained (Table 1); the space group was restricted to C222 or Cmmm. The orientational and positional orders of [C_{10}mim][NO_3]

were not alternatively obtained due to a lack of the Bragg reflections in the large unit cell. The minimum temperature (T_{min}) was 150 K in the LT X-ray diffraction. Using the X-ray diffraction pattern at T_{min}, the additional phase transition was not detected at $T_{min} < T < T_{C2}$. Consequently, the C_I-C_{II} crystal polymorph was observed in [C_{10}mim][NO_3] upon cooling.

Fig. 1(b) shows the phase transition upon heating. The reverse C_{II}-C_I phase transition occurred at 240 K (T_{C2}), and the hysteresis of the phase transition was found to be 20 K. The phase transition in LT [C_{10}mim][NO_3] is regarded as a weak first-order phase transition because of the small hysteresis. The Q_2 peak disappeared at T_{C2}, while the Q_{LC} Bragg reflection was detected again. The Q_{LC} peak shifted inversely to the higher Q position with increasing temperature. Hence, the shift of the Q_{LC} peak during cooling and heating cycles is considered as the distinctive characteristic of the C_I phase. The C_I phase melted at 290 K (T_m). Above T_m, the broad prepeak in the L phase appeared at Q_{pre} (Fig. 1(b)). In the thermal cycle, a reversible crystal polymorph was first observed in [C_{10}mim][NO_3] by the synchrotron radiation experiments. In case of LT 1-alkyl-3-methylimidazolium perfluorobutanesulfonate, [$C_n$mim][PFBS] (n = 4, 6, and 8) [34], irreversible crystal polymorphs were observed. Moreover, it was found that the conformational changes of both the cations and anion induced additional crystal phases at LT [37]. In contrast, the conformational degrees of freedom of the [C_{10}mim]$^+$ cation could be restricted to favoring the alkyl chain packing. Therefore, an additional crystal phase was suppressed in [C_{10}mim][NO_3] at LT.

3.2. HP phase behavior of [C_{10}mim][NO_3] at ambient temperature

At room temperature, phase transitions of [C_{10}mim][NO_3] under HP were initially studied using synchrotron radiation experiments. Fig. 2 (a) and 2(b) reveal the X-ray diffraction patterns upon compression and decompression, respectively. The observed and calculated X-ray diffraction patterns are shown by the black and colored curves, respectively. The optical microscope image showed that crystal domains developed inside the liquid at 0.7 GPa (P_{C1}) (Fig. 3). The distinct Debye rings were detected on the IP. As shown in Fig. 2(a), at P_{C1}, the HP crystal (α phase) provided an entirely different X-ray diffraction pattern compared with those of the LT phases (Fig. 1(a)). Moreover, a novel discovery of HP crystal structures was obtained in [C_{10}mim][NO_3]. The features of the α phase are (i) the 00ℓ Bragg reflections denoted by red closed circles, and (ii) double peak at low Q. In (i), the 001 Bragg reflection at the lowest Q did not overlap the prepeak at Q_{pre}, denoted by the blue closed circle in Fig. 2(a). The double peak consisted of the 2.7 nm^{-1} and 002 Bragg peaks. The 2.7 nm^{-1} peak was not equivalent to Q_{pre} or Q_2. By the structure analysis, the crystal structure of the α phase was orthorhombic (Table 1). The large unit cell can explain the

Table 1
Crystallographic data of [C_{10}mim][NO_3].

T (K)			a (nm)	b (nm)	c (nm)	α (°)	β (°)	γ (°)	Z	ρ (g/cm^3)	R_w (%)	R (%)
220	P422	C_I	1.5673	1.5673	4.3047	90	90	90	26	1.165	10.55	5.31
150	C222	C_{II}	1.3381	5.0703	4.2394	90	90	90	72	1.186	8.61	4.07
P (GPa)			a (nm)	b (nm)	c (nm)	α (°)	β (°)	γ (°)	Z	ρ (g/cm^3)	R_w (%)	R (%)
0.7	Imm2	A	1.5445	4.1751	8.6423	90	90	90	144	1.224	10.96	9.84
1.0	Imm2	A	1.5446	4.1633	8.5723	90	90	90	144	1.238	9.91	6.93
1.6	Imm2	β	1.0083	4.1901	8.4609	90	90	90	96	1.273	9.51	7.85
2.5	Imm2	β	0.9988	4.1781	8.3949	90	90	90	96	1.298	9.26	7.71
4.4	Imm2	γ	0.5084	4.0897	8.3113	90	90	90	48	1.316	12.59	12.54
5.5	Imm2	γ	0.5151	4.0645	8.2288	90	90	90	48	1.320	11.40	14.91
7.1	Imm2	γ	0.5148	4.0453	8.2138	90	90	90	48	1.330	12.00	15.40
8.3	Imm2	γ	0.5069	4.0449	8.2151	90	90	90	48	1.350	12.00	15.42
4.4	Imm2	γ	0.5011	4.1143	8.3206	90	90	90	48	1.326	12.44	10.85
3.9	Imm2	β	1.0037	4.1600	8.3644	90	90	90	96	1.302	8.06	8.14
2.6	Imm2	β	0.9971	4.1433	8.5791	90	90	90	96	1.283	5.27	5.29
1.2	Imm2	α	1.5447	4.1361	8.6653	90	90	90	144	1.232	7.16	6.07

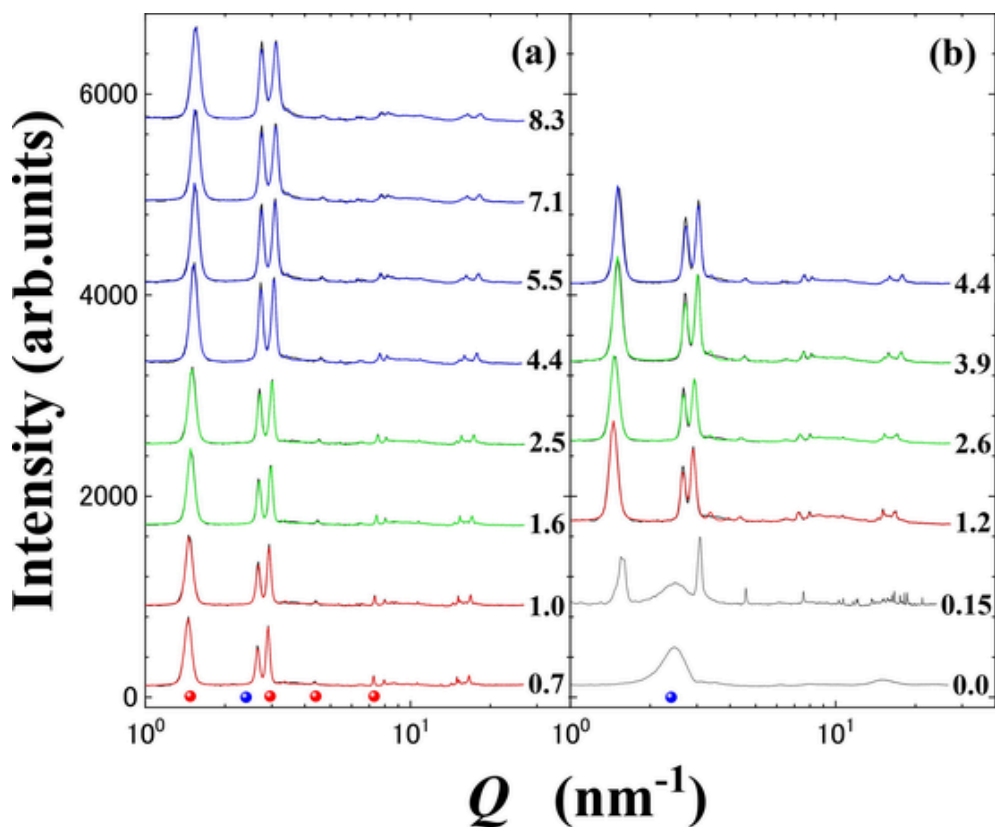**Fig. 2.** Pressure dependences of X-ray diffraction patterns in $[C_{10}mim][NO_3]$ upon (a) compression, and (b) decompression. Red closed circles indicate the 00ℓ Bragg reflections of the hybrid-layered structure. The blue closed circle reveals a prepeak position (Q_{pre}). The numbers in the figure indicate pressure (GPa).
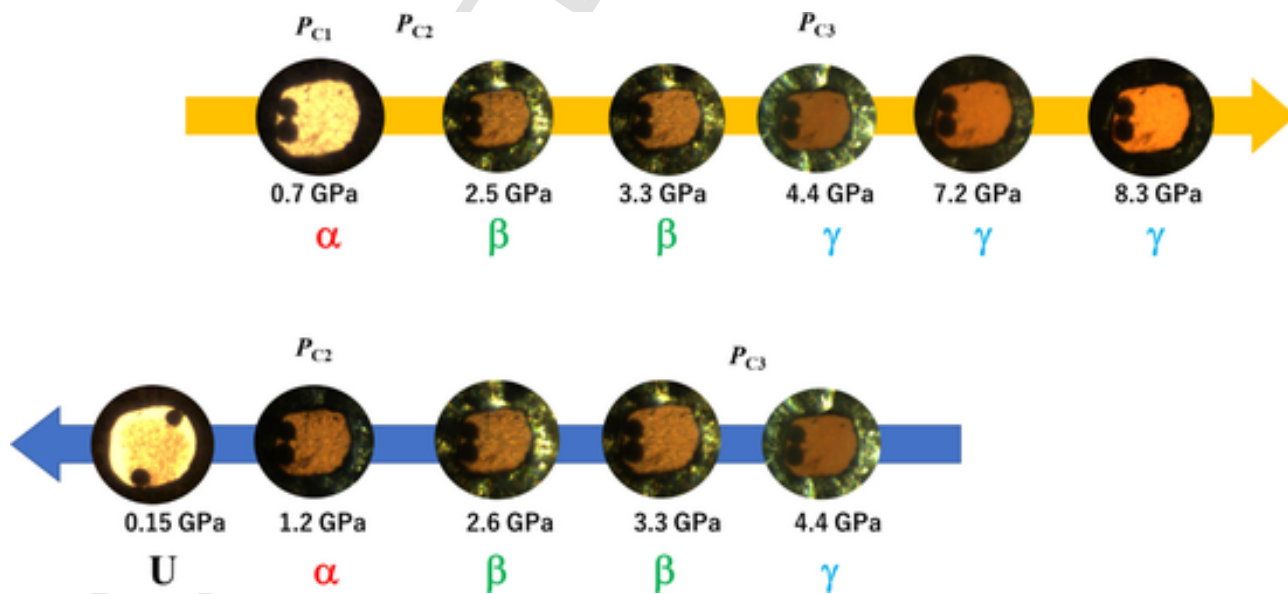

Fig. 3. Images of the diamond anvil cell (DAC) upon compression and decompression. Two ruby balls were inserted into the DAC.

observed 00ℓ Bragg reflections and the double peak. Previously, a double peak at low Q was observed in HP $[C_{10}mim][Br]$ [46]. The double peak in HP $[C_{10}mim][Br]$ existed in the absence of 00ℓ Bragg reflections. In HP $[C_{10}mim][Br]$, the double peak was linked to the large unit cell via a 3D network structure. For HP $[C_{10}mim][NO_3]$, the simultaneous appearance of the above (i) and (ii) features resulted in a relatively large unit cell (Table 1). Despite the large unit cell, the α phase structure was not identified uniquely due to a lack of Bragg reflections. The

unit cell at 0.7 GPa is illustrated in Fig. S1(b) as an example of α phase structure with a double peak. Compared with the unit cell of the 2D layered structure (LT C_I phase in Fig. S1(a)), the 3D network developed in the HP α phase of $[C_{10}mim][NO_3]$ (Fig. S1(b)). The α phase existed even at 1.0 GPa (Fig. 2(a)). At 1.6 GPa (P_{C2}), the weak Bragg reflections abruptly vanished. This new phase is called β phase, characterized by a smaller lattice constant, a (Table 1). By further compression, the crystal domain boundaries in Fig. 3 became ambiguous at 4.4 GPa (P_{C3}), as ob-

served by the optical microscope. A new γ phase appeared at P_{C3}. Although the 001 Bragg reflection and double peak at low Q were still sharp, the Bragg reflections at the high Q region representing the (hk0) plane became broad. Moreover, at P_{C3}, the peak splitting of the double peak increased, and the intensity ratio of the double peak varied, along with lowering of the lattice constant (Table 1). As listed in Table 1, the specific relation of a in the α, β, and γ phases was fond under HP. Here, the a lattice constant at P_{C3} (γ phase) is denoted, a_γ ($\approx$ 0.5 nm). The lattice constants of the α phase ($P < P_{C2}$) and β phase ($P_{C2} < P < P_{C3}$) are expressed by $3a_\gamma$ and $2a_\gamma$, respectively. Although the stacking sequence was preserved, the molecular orientation and position arrangements on the (hk0) plane became disorder as the unit cell was reduced. The maximum pressure (P_{max}) in the pressure cycle was 8.3 GPa. In Fig. 3, the sample at 7.2 GPa (P_g) and P_{max} was transparent, as evidenced in a glassy state of [C$_4$mim][PF$_6$] [27]. If we consider that some partial amorphization could occur inside the (hk0) plane with orientational disordering of [C$_{10}$mim]$^+$, the transparent sample featuring the partial amorphization did not contradict the peak broadening of the hk0 Bragg reflections at high Q in Fig. 2(a). In contrast, the γ phase was present even above P_g with the sharp 001 Bragg reflection and double peak. Consequently, α-β-γ phase transitions occurred in the compression process by reduction in the unit cell sizes, and the HP crystal structures differed from LT ones.

Generally, the second-order Birch-Murnaghan (BM) equation expresses compression as a function of pressure [47]. The second-order BM equation is provided by,

$$P = \frac{3}{2}K\left\{\left(\frac{V_0}{V}\right)^{\frac{7}{3}} - \left(\frac{V_0}{V}\right)^{\frac{5}{3}}\right\}, \tag{1}$$

where K is the isothermal bulk modulus. Blow P_{C2} ($=1.6$ GPa), compression was well fitted using the BM equation (Fig. 4). The bulk modulus below P_{C2} was found approximately to be 20 GPa, expressed by the grey curve in Fig. 4. The bulk modulus of [C$_{10}$mim][NO$_3$] was comparable to that of the flexible MOFs [4,48]. Hence, the α phase is regarded as the flexible crystal. It is noteworthy that the flexible MOF having a large pore transformed to the rigid crystal having a narrow pore, with changing the molecular conformations [48]. Similarly, above P_g, the
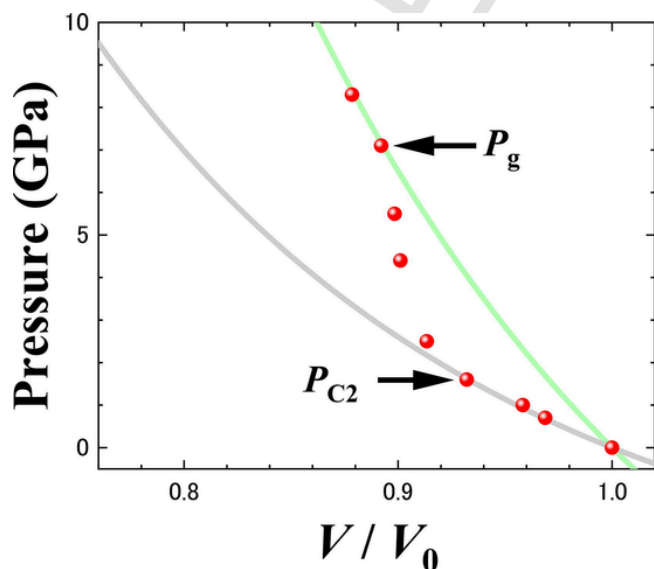

Fig. 4. Pressure increment by the isothermal bulk modulus. Two solid curves are calculated using second-order Birch–Murnaghan equation. The grey and green curves were calculated using bulk moduli of 20 GPa and 50 GPa, respectively.

bulk modulus of 50 GPa in [C$_{10}$mim][NO$_3$] was obtained by extrapolating the observed values (the green curve in Fig. 4). In case of [C$_{10}$mim][NO$_3$], the flexible–rigid phase transition was also induced under HP. Considering the hk0 Bragg peak broadening (Fig. 2) and the partial amorphization (Fig. 3) above P_g, disordering could promote the densely packing at HP. In the previous study [27], the disordering and densely packing were also seen in HP [C$_4$mim][PF$_6$]. It was considered that the partial amorphization of [C$_4$mim][PF$_6$] is caused by the folded cationic conformers and their orientational disorder. A concept of the conformational glass was introduced to explain the experimental results in [C$_4$mim][PF$_6$]. By referring the previous study [27], HP phase behaviors of [C$_{10}$mim][NO$_3$] were systematically interpreted by the densely packed and rigid phase, where conformational disordering, orientational disorder on the (hk0) planes, and partial amorphization are regarded as HP-inherent factors. Consequently, on the compression plot (Fig. 4), HP regime is divided into the three pressure regions: (i) the flexible IL below P_{C2}, (ii) the rigid IL above P_g, and (iii) the transient region between P_{C2} and P_g.

Fig. 2(b) depicts X-ray diffraction patterns upon decompression. A phase transition did not occur at 4.4 GPa; hence, the γ phase was stable with the disordering inside the (hk0) plane down to 4.4 GPa. A reversible γ-β phase transition was observed at 3.9 GPa (P_{C3}), and the crystal domain boundaries became distinct, as shown in Fig. 3. The hysteresis of the HP phase transition was minimal, similar to the LT phase transitions. This led to the discovery that the HP phase transition is also a weak first-order phase transition. The β phase appeared subsequently at 2.6 GPa and later transformed to the α phase by further decompression at 1.2 GPa (Fig. 2(b)). More importantly, the optical microscope revealed a noticeable morphological change at 0.15 GPa (Fig. 3). It should be noted that the domain wall motion led to the movement of the ruby balls (Fig. 3). The preferred orientation of the Debye rings was discovered on the IP. Thus, the crystal structure at 0.15 GPa was not resolved due to the strong preferred orientation. The U phase denotes the unknown crystal phase. At 0.15 GPa, a phase transition occurred, and a prepeak was superimposed in the X-ray diffraction pattern resulting in the coexistence of L and U phases in Fig. 2(b). Finally, the crystal melted completely at 0 GPa with the disappearance of the Bragg reflections. Without considering the U phase, an ideal and reversible crystal polymorph (α → β → γ → β → α) was also obtained in HP [C$_{10}$mim][NO$_3$]. Here, we emphasize that [C$_{10}$mim][NO$_3$] is regarded as an ideal and reversible crystal polymorph at both LT under ambient pressure and HP under ambient temperature, although the HP crystal polymorph was different from the LT crystal polymorph (Table 1).

3.3. Complicated layered structures of [C$_n$mim][X]

The LT crystal structure of [C$_{10}$mim][NO$_3$] was predicted by MD simulations [39]. Moreover, at 270 K, a solid–solid phase transition was shown to occur in the simulation box. Two crystal structures of LT [C$_{10}$mim][NO$_3$] were estimated to be triclinic ($P\bar{1}$), having the all-*trans* conformers of [C$_{10}$mim]$^+$ [39]. The estimated X-ray diffraction pattern was superimposed on the observed pattern at 220 K using the lattice constants calculated from DFT (Fig. S2). The results of the DFT calculations cannot account for the low-Q Bragg reflections of the observed X-ray diffraction pattern. Hence, the calculated lattice constant, $c = 2.226$ nm, which merely represents an LC-like stacking sequence, was not achieved in LT [C$_{10}$mim][NO$_3$].

The IL crystals with large unit cells are classified to emphasize the structural anomalies of LT and HP [C$_{10}$mim][NO$_3$] (Table 2). The structural features are distinguished by the X-ray diffraction patterns, which are schematically illustrated in Fig. 5. Inherent properties in the ILs are extracted for various crystal structures of [C$_n$mim][X] in Table 2. The hybrid-layered structure was observed in HP [C$_6$mim][PFBS] at ambient temperature [35], with a relatively short alkyl chain length,

Table 2

Geometrical classification of the ionic liquids at low temperature (LT) under ambient pressure and high pressure (HP) under ambient temperature. Crystals are distinguished by the liquid crystal (LC)-based layered structure, the hybrid-layered structure, and the three-dimensional (3D) network structure.

Layered (00ℓ Bragg reflections)		Non-layered (double peak)
LC-based layered	Hybrid-layered	3D network
	HP [C$_6$mim][PFBS]	
LT [C$_{10}$mim][Cl]	HP [C$_{10}$mim][Cl]	
LT [C$_{10}$mim][Br]		HP [C$_{10}$mim][Br]
	LT [C$_{10}$mim][NO$_3$]	
	HP [C$_{10}$mim][NO$_3$]	

whereas no layered structure was observed in LT [C$_6$mim][PFBS] at ambient pressure [34]. Particularly at HP under ambient pressure, a long periodic structure was introduced by the various conformers of [C$_6$mim]$^+$. Focusing on the [C$_{10}$mim]$^+$-based ILs, the other HP-induced hybrid-layered structure was identified in [C$_{10}$mim][Cl] [28]. At ambient temperature, the HP hybrid-layered structure was made of the folding and stacking layers of [C$_{10}$mim]$^+$. In contrast, LT [C$_{10}$mim][Cl] at ambient pressure belonged to the LC-based layered structure (Table 2). [C$_{10}$mim][Br] was similarly classed as an LC-based layered structure at LT under ambient pressure (Table 2) [46]. The phase behavior of HP [C$_{10}$mim][Br] at ambient temperature differed from that of HP [C$_{10}$mim][Cl] at ambient temperature while being an identical halogen anion. For instance, the crystal structure of HP [C$_{10}$mim][Br] did not coincide with that of HP [C$_{10}$mim][Cl]. The HP structural discrepancy between [C$_{10}$mim][Cl] and [C$_{10}$mim][Br] is described by the double peak without the 00ℓ Bragg reflections, representing the 3D network (Fig. 5). Despite having same halogens, different molecular packings were realized at HP under ambient temperature.

The crystal structures of [C$_{10}$mim][NO$_3$] in this study are listed in Table 2 to emphasize the anomalous crystal phases. LT [C$_{10}$mim][NO$_3$] at ambient pressure is characterized by the 2D hybrid-layered structure. On the other hand, HP [C$_{10}$mim][NO$_3$] at ambient temperature was found to be a new type of crystal structure with the 00ℓ Bragg reflections and the double peak (Fig. 5). This is explained by the 3D network in the large unit cell (Fig. S1(b)). In Table 2, the LT and HP crystal structures of [C$_{10}$mim][NO$_3$] are categorized as novel-complicated lattice modulations compared with the other ILs. Moreover, the crystal structures possessed extremely large lattice constants, which implied the different orientational ordering in the unit cells.

4. Conclusions

The LT and HP phase transitions of [C$_{10}$mim][NO$_3$] were examined using synchrotron radiation experiments. The reversible crystal polymorph formed with small hysteresis in the LT cycle at ambient pressure. The hybrid-layered structure was observed in LT [C$_{10}$mim][NO$_3$]. The abnormal peak shift of Q_{LC} peak showed lattice modulation of the C$_I$ phase. A more complicated crystal polymorph was observed at HP under ambient temperature. The 00ℓ Bragg reflections (hybrid-layered structure) and the double peak identified non 2D layered structure of HP [C$_{10}$mim][NO$_3$]. The crystal structures of HP [C$_{10}$mim][NO$_3$] possessed an extremely long lattice constant, permitting lattice modulations. Partial amorphization occurred above P_g. Using the BM equation, flexible and rigid bulk moduli were identified below P_{C2} and above P_g, respectively. The HP crystal polymorph was influenced by the flexible and rigid phase transition. HP small hysteresis and reversible phase transition, combined with LT small hysteresis, suggest that [C$_{10}$mim][NO$_3$] is a weak first-order phase transition. Due to the packing efficiency, the HP crystal polymorph at ambient temperature differed from the LT crystal polymorph at ambient pressure. Compared with other [C$_{10}$mim][X] systems, the LT and HP phase behaviors of [C$_{10}$mim][NO$_3$] were regarded as a new group of phase transitions, representing intricate molecular interactions.

CRediT authorship contribution statement

Hiroshi Abe : Conceptualization, Writing – original draft, Writing – review & editing. **Yuto Yoshiichi :** Data curation. **Hiroaki Kishimura :** Data curation. **Hajime Sagayama :** Data curation.

Declaration of Competing Interest

The authors declare that they have no known competing financial interests or personal relationships that could have appeared to influence the work reported in this paper.

Data availability

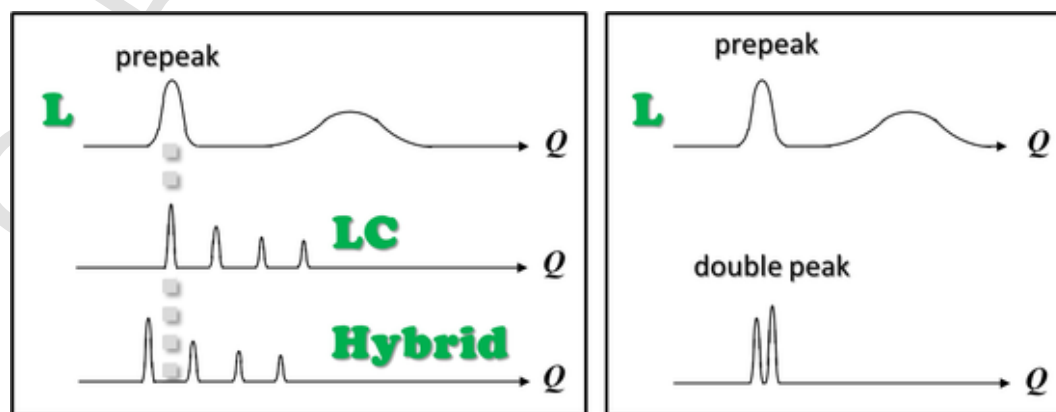Data will be made available on request.

Acknowledgments

Fig. 5. Schematic X-ray diffraction patterns in [C$_n$mim][X] at a low temperature under ambient pressure and high pressure under ambient temperature. The prepeak appeared in the liquid (L) phase. The liquid crystal (LC)-like crystal structure is characterized by the sharp Bragg reflection at the prepeak position. The hybrid-layered structure possessed a longer lattice constant along the stacking direction.

2019G006, 2020G598, and 2021G004). Crystal structures were displayed using *VESTA* 3 [49].

Appendix A. Supplementary data

Supplementary data to this article can be found online at https://doi.org/10.1016/j.cplett.2023.140685.

References

[1] S.K. Elsaidi, M.H. Mohamed, D. Banerjee, P.K. Thallapally, Flexibility in Metal-Organic Frameworks: A fundamental understanding, Coord. Chem. Rev. 358 (2018) 125–152.

[2] I.E. Collings, A.L. Goodwin, Metal–organic frameworks under pressure, J. Appl. Phys. 126 (2019) 181101–181113.

[3] J. Wieme, S.M.J. Rogge, P.G. Yot, L. Vanduyfhuys, S.-K. Lee, J.-S. Chang, M. Waroquier, G. Maurin, V. Van Speybroeck, Pillared-layered metal–organic frameworks for mechanical energy storage applications, J. Mater. Chem. A 7 (39) (2019) 22663–22674.

[4] P. Vervoorts, J. Keupp, A. Schneemann, C.L. Hobday, D. Daisenberger, R.A. Fischer, R. Schmid, G. Kieslich, Configurational entropy driven high-pressure behaviour of a flexible metal-organic framework (MOF), Angew. Chem. Int. Ed. 60 (2) (2021) 787–793.

[5] G.F. Turner, S.C. McKellar, D.R. Allan, A.K. Cheetham, S. Henke, S.A. Moggach, Guest-mediated phase transitions in a flexible pillared-layered metal–organic framework under high-pressure, Chem. Sci. 12 (41) (2021) 13793–13801.

[6] P. Zhao, S.C. Edman Tsang, D. Fairen-Jimenez, Structural heterogeneity and dynamics in flexible metal-organic frameworks, Cell Rep. Phys. Sci. 2 (2021) 100544–.

[7] R. Pallach, J. Keupp, K. Terlinden, L. Frentzel-Beyme, M. Kloß, A. Machalica, J. Kotschy, S.K. Vasa, P.A. Chater, C. Sternemann, M.T. Wharmby, R. Linser, R. Schmid, S. Henke, Frustrated flexibility in metal-organic frameworks, Nature Commun. 12 (2021) 4097–12.

[8] J.N.A. Canongia Lopes, A.A.H. Pádua, Nanostructural organization in ionic liquids, J. Phys. Chem. B 110 (2006) 3330-3335.

[9] A. Triolo, O. Russina, H.-J. Bleif, E. Di Cola, Nanoscale segregation in room temperature ionic liquids, J. Phys. Chem. B 111 (18) (2007) 4641–4644.

[10] J.D. Holbrey, K.R. Seddon, Ionic liquids, Clean Prod. Proc. 1 (1999) 223–236.

[11] J.D. Holbrey, W.M. Reichert, R.D. Rogers, Crystal structures of imidazolium bis (trifluoromethanesulfonyl)-imide 'ionic liquid' salts: the first organic salt with a cis-TFSI anion conformation, Dalton Trans. (2004) 2267–2271.

[12] F. Nemoto, M. Kofu, O. Yamamuro, Thermal and Structural studies of imidazolium-based ionic liquids with and without liquid-crystalline phases: the origin of nanostructure, J. Phys. Chem. B 119 (2015) 5028–5034.

[13] K. Binnemans, Ionic liquid crystals, Chem. Rev. 105 (11) (2005) 4148–4204.

[14] T. Ichikawa, M. Yoshio, A. Hamasaki, T. Mukai, H. Ohno, T. Kato, Self-organization of room-temperature ionic liquids exhibiting liquid-crystalline bicontinuous cubic phases: formation of nano-ion channel networks, J. Am. Chem. Soc. 129 (2007) 10662–10663.

[15] J. Sakuda, M. Yoshio, T. Ichikawa, H. Ohno, T. Kato, 2D assemblies of ionic liquid crystals based on imidazolium moieties: formation of ion-conductive layers, New J. Chem. 39 (2015) 4471–4477.

[16] K. Goossens, K. Lava, C.W. Bielawski, K. Binnemans, Ionic liquid crystals: versatile materials, Chem. Rev. 116 (2016) 4643–4807.

[17] T. Ichikawa, Zwitterions as building blocks for functional liquid crystals and block copolymers, Polymer J. 49 (5) (2017) 413–421.

[18] Y. Biswas, P. Banerjee, T.K. Mandal, From polymerizable ionic liquids to poly (ionic liquid)s: structure-dependent thermal, crystalline, conductivity, and solution thermoresponsive behaviors, Macromolecules 52 (2019) 945–958.

[19] X. Qiao, P. Sun, A. Wu, N. Sun, B. Dong, L. Zheng, Supramolecular thermotropic ionic liquid crystals formed via self-assembled zwitterionic ionic liquids, Langmuir 35 (2019) 1598–1605.

[20] K. Salikolimi, A.A. Sudhakar, Y. Ishida, Functional ionic liquid crystals, Langmuir 36 (2020) 11702–11731.

[21] N. Kapernaum, A. Lange, M. Ebert, M.A. Grunwald, C. Haege, S. Marino, A. Zens, A. Taubert, F. Giesselmann, S. Laschat, Current topics in ionic liquid crystals, ChemPlusChem 87 (2022) e202100397–e202100438.

[22] O. Renier, G. Bousrez, K. Stappert, M. Wilk-Kozubek, B. Adranno, H. Pei, E.T. Spielberg, V. Smetana, A.-V. Mudring, Photoisomerization and mesophase formation in azo-ionic liquids, Cryst. Growth Des. 20 (2020) 214–225.

[23] K. Tanabe, Y. Suzui, M. Hasegawa, T. Kato, Full-color tunable photoluminescent ionic liquid crystals based on tripodal pyridinium, pyrimidinium, and quinolinium salts, J. Am. Chem. Soc. 134 (2012) 5652–5661.

[24] K. Iakoubovskii, M. Yoshio, Room-temperature zwitterionic liquid crystals for mechanical actuators, ACS Mater. Au 2 (6) (2022) 686–689.

[25] H. Abe, N. Hamaya, Y. Koyama, H. Kishimura, T. Takekiyo, Y. Yoshimura, D.

[26] Wakabayashi, N. Funamori, K. Matsuishi, Long periodic structure of a room-temperature ionic liquid by high-pressure small-angle X-ray scattering and wide-angle X-ray scattering: 1-decyl-3-methylimidazolium chloride, ChemPhysChem 19 (2018) 1441–1447.

[26] T. Endo, T. Kato, K. Tozaki, K. Nishikawa, Phase behaviors of room temperature ionic liquid linked with cation conformational changes: 1-butyl-3-methylimidazolium hexafluorophosphate, J. Phys. Chem. B 114 (2010) 407–411.

[27] H. Abe, T. Takekiyo, N. Hatano, M. Shigemi, N. Hamaya, Y. Yoshimura, Pressure-induced frustration−frustration process in 1-butyl-3-methylimidazolium hexafluorophosphate, a room-temperature ionic liquid, J. Phys. Chem. B 118 (2014) 1138–1145.

[28] S. Saouane, S.E. Norman, C. Hardacre, F.P.A. Fabbiani, Pinning down the solid-state polymorphism of the ionic liquid [bmim][PF$_6$], Chem. Sci. 4 (2013) 1270–1280.

[29] O. Russina, B. Fazio, C. Schmidt, A. Triolo, Structural organization and phase behaviour of 1-butyl-3-methylimidazolium hexafluorophosphate: an high pressure Raman spectroscopy study, Phys. Chem. Chem. Phys. 13 (2011) 12067–12074.

[30] T. Endo, H. Masu, K. Fujii, T. Morita, H. Seki, S. Sen, K. Nishikawa, Determination of missing crystal structures in the 1-alkyl-3-methylimidazolium hexafluorophosphate series: implications on structure−property relationships, Cryst. Growth Des. 13 (12) (2013) 5383–5390.

[31] S. Hayashi, R. Ozawa, H. Hamaguchi, Raman spectra, crystal polymorphism, and structure of a prototype ionic-liquid [bmim]Cl, Chem. Lett. 32 (2003) 498–499.

[32] J.D. Holbrey, W. Matthew Reichert, M. Nieuwenhuyzen, S. Johnston, K.R. Seddon, R.D. Rogers, Crystal polymorphism in 1-butyl-3-methylimidazolium halides: supporting ionic liquid formation by inhibition of crystallization, Chem. Commun. (2003) 1636–1637.

[33] W.A. Henderson, P. Fylstra, H.C. De Long, P.C. Trulove, S. Parsons, Crystal structure of the ionic liquid EtNH$_3$NO$_3$—Insights into the thermal phase behavior of protic ionic liquids, Phys. Chem. Chem. Phys. 14 (2012) 16041–16046.

[34] Y. Koyama, S. Shimono, H. Abe, K. Matsuishi, Crystal polymorphs in 1-alkyl-3-methylimidazolium perfluorobutanesulfonate ionic liquids, J. Mol. Liq. 317 (2020) 113908–7.

[35] H. Abe, Y. Koyama, S. Shimono, H. Kishimura, K. Matsuishi, High-pressure crystal polymorphs and multiple pathways in 1-hexyl-3-methylimidazolium perfluorobutanesulfonate ionic liquid, Chem. Phys. 557 (2022) 111479–7.

[36] T. Endo, T. Higuchi, Y. Kimura, DFT study on conformation of 1-alkyl-3-methylimidazolium with ethyl, propyl, butyl, pentyl, and hexyl group, Bull. Chem. Soc. Jpn. 93 (6) (2020) 720–729.

[37] H. Abe, H. Kishimura, M. Uruichi, A phase variety of fluorinated ionic liquids: Molecular conformational and crystal polymorph, Spectrochim. Acta A 286 (2023) 121948–7.

[38] E. Patyk-Kaźmierczak, M. Kaźmierczak, A new high-pressure benzocaine polymorph — towards understanding the molecular aggregation in crystals of an important active pharmaceutical ingredient (API), Acta Crystallogr. B 76 (1) (2020) 56–64.

[39] W. Cao, Y. Wang, G. Saielli, Metastable state during melting and solid-solid phase transition of [C$_n$Mim][NO$_3$] (n = 4–12) IONIC LIQUIDS BY MOLECULAR DYNAMICS SIMULATion, J. Phys. Chem. B 122 (1) (2018) 229–239.

[40] W. Cao, Y. Wang, Phase behaviors of ionic liquids heating from different crystal polymorphs toward the same smectic-A ionic liquid crystal by molecular dynamics simulation, Crystals 9 (2019) 26–14.

[41] S. Li, Y. Wang, Percolation phase transition from ionic liquids to ionic liquid crystals, Sci. Rep. 9 (2019) 13169–8.

[42] H. Abe, H. Kishimura, Multistep phase transition in 1-decyl-3-methylimidazolium nitrate ionic liquid, J. Mol. Liq. 352 (2022) 118695–118698.

[43] O. Shimomura, K. Takemura, H. Fujihisa, Y. Fujii, T. Ohishi, T. Kikegawa, Y. Amemiya, T. Matsushita, Application of an imaging plate to high-pressure X-ray study with a diamond anvil cell, Rev. Sci. Instrum. 63 (1992) 967–973.

[44] R. Oishi-Tomiyasu, Robust powder auto-indexing using many peaks, J. Appl. Cryst. 47 (2014) 593–598.

[45] V. Favre-Nicolin, R. Cerny, *FOX*, 'free objects for crystallography': a modular approach to *ab initio* structure determination from powder diffraction, J. Appl. Crystallogr. 35 (2002) 734–743.

[46] H. Abe, Y. Yoshiichi, H. Kishimura, Low-temperature and high-pressure phase transitions of ionic liquid: 1-decyl-3-methylimidazolium bromide, to be submitted in ChemistrySelect.

[47] T. Katsura, Y. Tange, A simple derivation of the Birch–Murnaghan equations of state (EOSs) and comparison with EOSs derived from other definitions of finite strain, Minerals 9 (2019) 745-18.

[48] J. Navarro-Sánchez, I. Mullor-Ruíz, C. Popescu, D. Santamaría-Pérez, A. Segura, D. Errandonea, J. González-Platas, C. Martí-Gastaldo, Peptide metal–organic frameworks under pressure: flexible linkers for cooperative compression, Dalton Trans. 47 (2018) 10654–10659.

[49] K. Momma, F. Izumi, VESTA 3 for three-dimensional visualization of crystal, volumetric and morphology data, J. Appl. Crystallogr. 44 (2011) 1272–1276.